How to cite: *Angew. Chem. Int. Ed.* **2021**, *60*, 17664–17670
International Edition: doi.org/10.1002/anie.202105512
German Edition: doi.org/10.1002/ange.202105512

Perovskite Solar Cells

Robust Molecular Dipole-Enabled Defect Passivation and Control of Energy-Level Alignment for High-Efficiency Perovskite Solar Cells

Bing Wang, Hong Li, Qingqing Dai, Meng Zhang, Zhigang Zou, Jean-Luc Brédas,* and Zhiqun Lin**

Abstract: *The ability to passivate defects and modulate the interface energy-level alignment (IEA) is key to boost the performance of perovskite solar cells (PSCs). Herein, we report a robust route that simultaneously allows defect passivation and reduced energy difference between perovskite and hole transport layer (HTL) via the judicious placement of polar chlorine-terminated silane molecules at the interface. Density functional theory (DFT) points to effective passivation of the halide vacancies on perovskite surface by the silane chlorine atoms. An integrated experimental and DFT study demonstrates that the dipole layer formed by the silane molecules decreases the perovskite work function, imparting an Ohmic character to the perovskite/HTL contact. The corresponding PSCs manifest a nearly 20% increase in power conversion efficiency over pristine devices and a markedly enhanced device stability. As such, the use of polar molecules to passivate defects and tailor the IEA in PSCs presents a promising platform to advance the performance of PSCs.*

Introduction

The past two decades have witnessed remarkable advances in perovskite solar cells (PSCs) with their power conversion efficiency (PCE) leaping from 3.8% to a recently certified 25.5%.[1] The ability to decrease the density of defects (e.g., deep defects—Pb-I antisites and Pb clusters,[2] and shallow defects—halide vacancies and interstitials)[3] and grain boundaries (GBs) represents an effective route to improving carrier transport and collection and increasing the PSC efficiency. As defects function as photoluminescence quenching sites and lead to charge trap states, they worsen the non-radiative losses in the devices and limit performance.[4] Moreover, the presence of GBs increases ion migration due to higher ion diffusivity across GBs.[5] In this context, various routes to passivating defects and GBs have emerged.[2a,3,6] For instance, the incorporation of halide atoms at the perovskite/electron transport layer (ETL) interface can lower the density of interfacial trap states due to the passivation of Pb-I antisite defects and halide vacancies (V_X; where X = Br and I).[2a] Moreover, quaternary ammonium halides (e.g., choline chloride and choline iodide) are found to reduce the charge trap density induced by cationic (Pb clusters) and anionic defect sites (PbI_3^- antisite defects) at the perovskite/ETL interface.[2b] Clearly, the introduction of additional halide ions during the growth process of perovskite crystals is effective in passivating defects.[2]

In addition to defect passivation, modulating the interface energy-level alignment (IEA) represents another key factor that influences charge extraction and transport in PSCs.[7] Delicate control over the IEA between perovskite and ETL, as well as between perovskite and hole transport layer (HTL), affords efficient charge carrier transfer at the perovskite/ETL and perovskite/HTL interfaces and minimizes the open-circuit voltage (V_{OC}) loss in the device.[6a] Taken together, the ability to produce perovskite films with a much-reduced density of trap states and energetically favorable IEA is an essential prerequisite for high-efficiency PSCs.

Herein, we report a simple yet robust strategy to effectively and concurrently passivate defects and optimize IEA at the perovskite/HTL interface by judiciously positioning strongly polar chlorosilane molecules at the perovskite/HTL interface. A representative metal halide perovskite with mixed monovalent cations, $Cs_{0.06}FA_{0.79}MA_{0.15}Pb(I_{0.85}Br_{0.15})_3$, is chosen as the absorber.[4] Halide-terminated polar silanes, chloropropyltrimethoxysilane (CPS, $Cl\text{-}(CH_2)_3\text{-}Si\text{-}(OCH_3)_3$) and chloromethyltrimethoxysilane (CMS, $Cl\text{-}CH_2\text{-}Si\text{-}(OCH_3)_3$) (Figure S1), are selected as the passivation molecules and deposited on the surface of the perovskite film. The corresponding films are systematically characterized by scanning electron microscopy (SEM), UV-vis absorption, steady-state photoluminescence (PL), time-resolved photoluminescence (TRPL), ultraviolet photoelectron spectroscopy (UPS), atomic force microscopy (AFM), X-ray diffraction (XRD), and contact angle camera. Density functional theory (DFT) calculations are performed to assess the role the CPS passivation layer plays on modulating the surface work function and interface energy-level alignment. Also, the

[*] Dr. B. Wang, Dr. M. Zhang, Prof. Dr. Z. Lin
School of Materials Science and Engineering Atlanta, Georgia Institute of Technology
Atlanta, GA 30332 (USA)
E-mail: zhiqun.lin@mse.gatech.edu
Dr. H. Li, Dr. Q. Dai, Prof. Dr. J. Brédas
Department of Chemistry and Biochemistry, The University of Arizona
Tucson, AZ 85721-0088 (USA)
E-mail: jlbredas@arizona.edu
Dr. B. Wang, Prof. Dr. Z. Zou
Eco-materials and Renewable Energy Research Center, School of Physics, Nanjing University
Nanjing 210093 (P. R. China)
E-mail: zgzou@nju.edu.cn
Supporting information and the ORCID identification number(s) for the author(s) of this article can be found under: https://doi.org/10.1002/anie.202105512.

current density-voltage (*J-V*) characteristics of PSC devices are measured under AM 1.5G irradiation.

The silane-treated PSCs present a *PCE* of 20.3%, which represents a nearly 20% efficiency increase over the pristine counterpart (*PCE* = 17.1%). Importantly, such a significant improvement of performance is also achieved in silane-treated $MAPbI_3$-based device, further demonstrating the effectiveness of CPS and CMS layers in passivating defects and improving IEA. Also, we find that the device stability is significantly enhanced after passivation.

Results and Discussion

It has been reported that chlorine-containing molecules are more suitable than other halides for passivating defects in perovskites due to the stronger Pb–Cl bonding over Pb–I or Pb–Br bonding.[8] Moreover, it has been demonstrated that Cl-rich nucleation sites lead to better crystal coalescence and minimized GBs,[9] and that the presence of chlorinated species around GBs reduces electron-hole recombination.[10] Also, the CPS and CMS chlorosilane molecules possess a strong dipole moment owing to the two terminal functional groups with the dipole moments pointing from -Cl to $-OCH_3$ ends. Thus, they can form a molecular dipole layer at the perovskite/HTL interface, which can be exploited to improve IEA for hole extraction and induce a higher V_{OC}. However, investigations into the use of silanes for defect passivation in order to optimize interfaces in PSCs have remained limited in scope, particularly in the context of the passivation mechanisms and the effect on IEA.

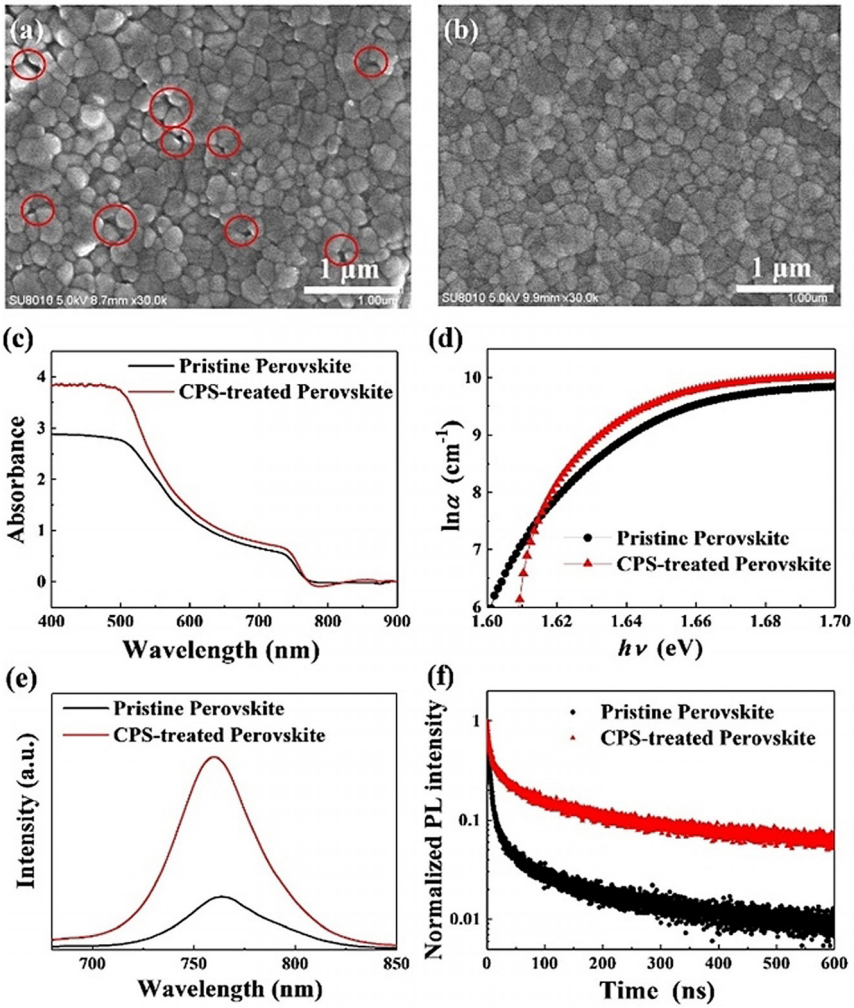

Figure 1. SEM images of $Cs_{0.06}FA_{0.79}MA_{0.15}Pb(I_{0.85}Br_{0.15})_3$ films a) without and b) with CPS treatment. The red circles indicate the gaps between perovskite crystals. c) UV-vis absorption spectra, d) dependence of $\ln\alpha$ on photon energy ($h\nu$), e) steady-state PL spectra, and f) TRPL of pristine and CPS-treated perovskite films on bare glass.

Unless otherwise specified, the perovskite used in our study is $Cs_{0.06}FA_{0.79}MA_{0.15}Pb(I_{0.85}Br_{0.15})_3$. Figure 1a,b compares the SEM images of $Cs_{0.06}FA_{0.79}MA_{0.15}Pb(I_{0.85}Br_{0.15})_3$ films without and with CPS silane treatment. The deposition of CPS appears to tighten the proximity of perovskite crystallites, while many gaps between crystallites (marked with red cycles in Figure 1a) are found in the pristine perovskite film. Figure S2 shows the atomic force microscopy (AFM) height images of the $Cs_{0.06}FA_{0.79}MA_{0.15}Pb(I_{0.85}Br_{0.15})_3$ films before and after CPS treatment. The root-mean-square roughness (R_q) of the film decreases in half, from 24.2 nm in the pristine sample to 12.0 nm after CPS deposition, which points to CPS passivating the GBs and reducing the height difference between the crystallite surface and the GB.

The absorbance of the CPS-treated perovskite film increases over the entire visible range, implying an enhanced light-harvesting capacity (Figure 1c). Figure 1d displays *ln* α (where α is the absorption coefficient) versus photon energy near the absorption edge. For the CPS-treated perovskite film, the Urbach energy E_U (ca. 10 meV), as determined by the reciprocal of the slope of straight lines near the absorption edge, is lower than that of the pristine film (ca. 15 meV) (see *Supplementary Note 1* in *Supporting Information*).[11] This result suggests that the density of trap states in the perovskite film is reduced upon CPS treatment.[12] The steady-state photoluminescence (PL) spectra demonstrate that the PL intensity of the CPS-treated perovskite film is four times as large as that of the pristine film (Figure 1e), which indicates that the CPS treatment greatly reduces the trap-assisted recombination process and non-radiative losses.[13] The time-resolved photoluminescence (TRPL) decays of the two perovskite films deposited on bare glass can be fitted to a bi-exponential decay with a fast and a slow component (Figure 1f). The fast and slow quenching processes can be attributed to radiative recombination from bulk perovskite and non-radiative recombination by defects, respectively.[3,14]

Notably, the CPS-treated film displays longer lifetimes for both fast and slow processes, suggesting that the CPS treatment decreases defect-induced non-radiative recombination processes and improves the quality of the bulk perovskite film. This can be ascribed to the passivation of defects and GBs in the CPS-modified perovskite.

CPS has an intrinsic dipole moment with negative and positive poles on the -Cl and -OCH_3 ends, respectively.[15] Thus, it is susceptible to form a molecular dipole layer at the perovskite/HTL interface (i.e., $Cs_{0.06}FA_{0.79}MA_{0.15}Pb(I_{0.85}Br_{0.15})_3$/Spiro-OMeTAD; see *Experimental Section* in *Supporting Information*),[16] thereby altering the energy band alignment.[17] As the silane Cl atom can passivate some of the perovskite defects, the CPS molecules are expected to interact with the defects through their Cl ends. Earlier density-functional theory (DFT) calculations using the generalized gradient approximation without spin-orbit coupling have found that the formation energy of halide vacancies ($V_X = \approx 0.67$ eV) is lowest among defects including iodine interstitials (≈ 0.83 eV) and MA vacancies (≈ 1.28 eV).[18] Thus, V_X is anticipated to be the primary form of defects in perovskites and the chlorine atoms can be assumed to passivate such V_X sites (Figure 2a). Given this orientation, the electrostatic potential energy comes down above the dipolar interlayer (right panel, Figure 2b; Figure 2c).[16,17] Consequently, compared to the pristine perovskite, the energy difference Φ_b between the valence band maximum (VBM) of the perovskite and the HTL HOMO level decreases; this also means that the energy difference between the perovskite conduction band minimum (CBM) and the HTL HOMO increases upon CPS treatment, which contributes to raise the PSC V_{OC}. To confirm the validity of this assessment, we determined the band alignment between $Cs_{0.06}FA_{0.79}MA_{0.15}Pb(I_{0.85}Br_{0.15})_3$ and Spiro-OMeTAD. Figure 2b depicts the energy band diagram of the perovskite/HTL interface in the absence and in the presence of the molecular dipole layer. The perovskite energy levels were determined from ultraviolet photoelectron spectroscopy (UPS, Figure S3) and UV/Vis absorption measurements (Figure 1c), while the HTL-Spiro-OMeTAD levels ($E_{LUMO} = -2.24$ eV and $E_{HOMO} = -5.22$ eV) were taken from the literature.[19] The perovskite energy-level evolution after CPS passivation is consistent with our expectations. The work function decreases by ca. 0.35 eV due to the CPS dipole layer and Φ_b reduces from 0.42 eV to 0.01 eV, which results in an Ohmic contact; simultaneously, the energy difference between the perovskite CBM and the HTL HOMO increases from 1.21 eV to 1.62 eV. These results in turn verify that it is the Cl end of the CPS layer that binds to the perovskite surface.

To further understand the impact of the silane layer on passivating the perovskite surface defects and regulating the work function, we performed DFT calculations with the Perdew-Burke-Ernzerhof (PBE) functional and the Grimme dispersion correction (DFT-D2) (see the *Supporting Information* for details on the computational methodology). To facilitate the computational work, $MAPbI_3$ was selected as the perovskite material (we note that $MAPbI_3$-based devices without and with chlorosilane treatments were also fabricated and compared, see Figures S4–S5; the results demonstrate that in this case as well the incorporation of chlorosilane molecules significantly improves PSC performance). We considered two limiting cases: In the first one, the $MAPbI_3$ surface is considered to be perfectly terminated either by a MAI layer (Figure S6a) or by a PbI_2 layer (Figure S7a). In the other case, each surface unit cell contains an iodide vacancy (V_I), which corresponds to a surface defect density of 1.29×10^{14} cm^{-2} (Figure S6b and Figure S7b). The modification of each surface by a CPS monolayer (Figures S6c,6d and Figures S7c,7d) was then modeled to examine the change in

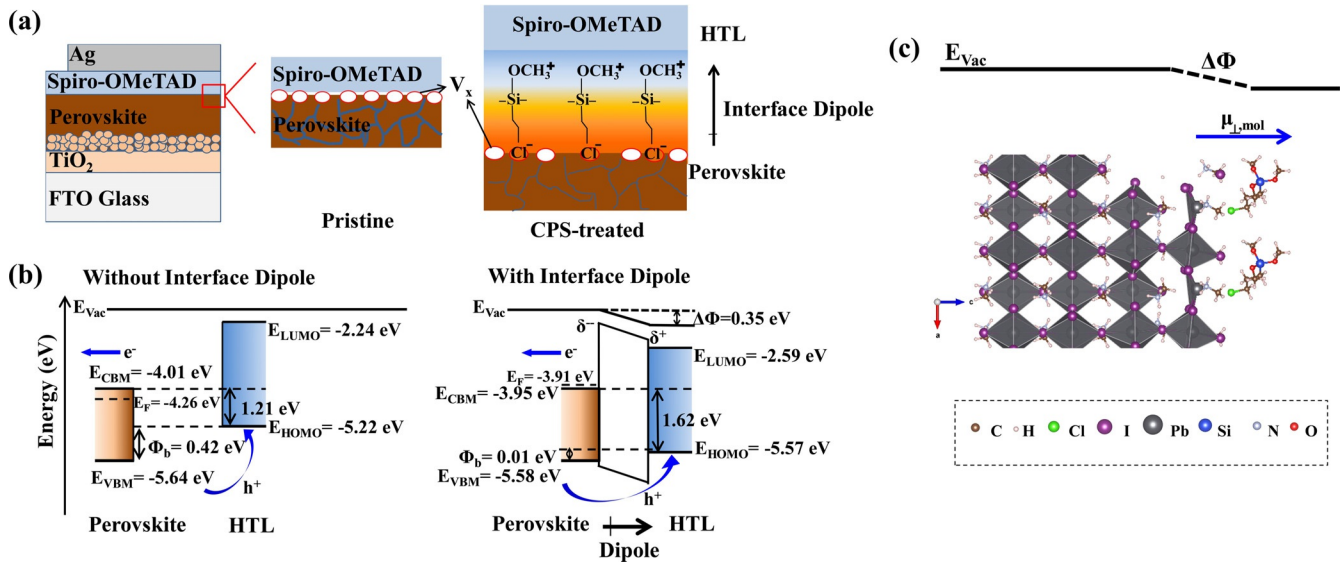

Figure 2. a) Schematic diagram of PSC without (central panel) and with (right panel) CPS treatment. The open red circles represent V_X sites. b) Schematic band diagram of perovskite/HTL (i.e., $Cs_{0.06}FA_{0.79}MA_{0.15}Pb(I_{0.85}Br_{0.15})_3$ and Spiro-OMeTAD) without and with interfacial dipole pointing towards HTL. Note, a rigid energy shift of the HOMO and the lowest unoccupied molecular orbital (LUMO) of the HTL was assumed caused by the change in E_{vac} after CPS treatment. c) Schematic energy level of perovskite and Spiro-OMeTAD as calculated at the DFT level.

work function (Φ) (Figures S8–S9). For both the MAI and PbI_2 surface terminations, the CPS molecules bind more strongly to the V_I-containing surfaces than the perfect surfaces. The binding energy per CPS molecule is approximately −0.42 eV for the MAI-terminated surface (MAI-V_I) and −0.72 eV for the PbI_2-terminated surface (PbI_2-V_I). These values are 0.19 eV and 0.29 eV larger than those for the respective perfect surface terminations (see the discussion of Figures S4–S5 in *Supporting Information*). The Cl atoms are found to point towards the V_I sites with the trimethoxy groups (OCH_3) away from the surface (Figure 2c), which corroborates the description in Figure 2a. The shortest distance between a CPS Cl atom and an under-coordinated Pb on the MAI-V_I surface is ≈3.70 Å, which is approximately 0.5 Å longer than the Pb–I bond length in the perovskite lattice. Overall, the results indicate that the CPS molecules are weakly adsorbed on the perovskite surface, with Cl atoms (partially) saturating and thus passivating the under-coordinated Pb cations associated with V_I sites.

The calculated work function changes ($\Delta\Phi$) for the CPS-modified MAI-V_I and PbI_2-V_I surfaces are −0.81 and −1.12 eV, respectively (Figures S8–S11), which is consistent with the experimental evolution (−0.35 eV in Figure 2a) measured by UPS. The fact that the absolute values of the calculated work function decrease are two to three times as large as the experimental result can be attributed to the high surface coverage of CPS molecules and high surface density of iodine vacancies modeled in the DFT study (which is a necessary step to prevent the computational costs to become prohibitive).

Using the methodology developed in our earlier work,[20] we explored the underlying mechanism for the work function decrease. Our calculations indicate that, for both the CPS-modified MAI-V_I and PbI_2-V_I surfaces, the main factor leading to the work function decrease is the electrostatic potential energy drop (ΔV_{mol}) induced by the dipolar CPS layer, −0.85 eV (Figure S8) and −0.82 eV (Figure S9) for the MAI-V_I and PbI_2-V_I surfaces, respectively. These electrostatic energy drops correspond to molecular dipoles with the components perpendicular to the surface ($\mu_{\perp,mol}$) calculated to be 1.68 and 1.74 Debye, respectively (Figure 2c).

The champion PSC fabricated with the CPS-treated perovskite shows improved performance (Figure 3a) with V_{OC} of 1.12 V, short-circuit current (J_{SC}) of 24.8 mA cm^{-2}, fill factor (*FF*) of 73%, and overall PCE of 20.3%. The average PCE over ten devices amounts to 19.2 ± 0.5%. These values can be compared to those for the control devices based on pristine perovskite films: the champion cell has V_{OC} of 1.06 V, J_{SC} of 24.1 mA cm^{-2}, *FF* of 67%, and *PCE* of 17.1%, while the average PCE value over ten cells is 16.9 ± 0.2%. The enhanced J_{SC} is due to improved light harvesting (Figure 1c), while the increase in both V_{OC} and *FF* are indicative of an improved morphology of the perovskite film (Figure 1b) as well as the passivation of defects and GBs, leading to a reduced non-radiative charge recombination in the perovskite film (Figure 1e). In addition, the CPS dipole layer at the interface between the perovskite and HTL layer results in a higher V_{OC}, as discussed above (Figure 2b).[21] It is also worth noting that the hysteresis in the CPS-based PSC was much smaller than that in the control device (Figure S12); the PCE of pristine perovskite-based devices drops by 1.1% when the scan direction switches from reverse to forward, while it only decreases by 0.6% for devices treated with CPS, which further confirms the lesser density of defects in the

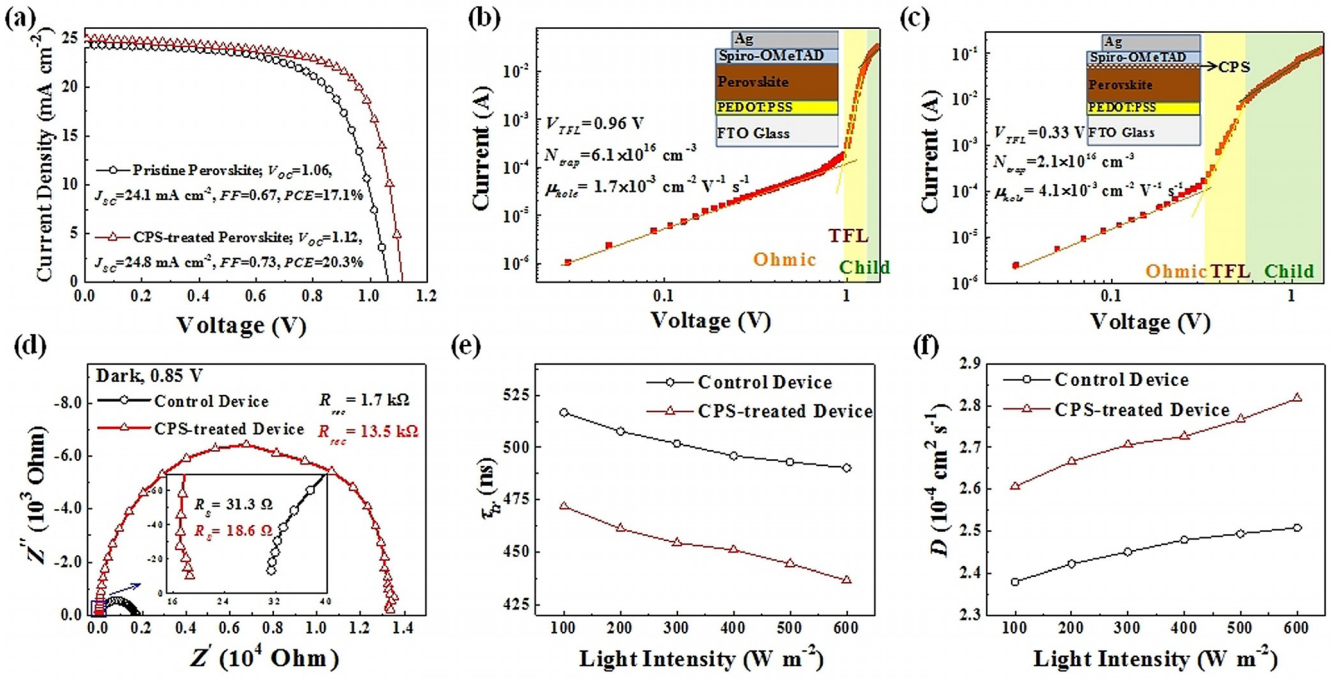

Figure 3. a) *J-V* curves of the champion PSC without and with CPS passivation. *I-V* characteristics of hole-only devices by using b) a pristine perovskite film and c) a CPS-treated perovskite film. d) Nyquist plots of electrochemical impedance spectroscopy (EIS) for the devices in the dark at an applied bias of 0.85 V. e) Charge carrier transfer time τ_{tr} and f) charge diffusion coefficient D_n as a function of light intensity.

CPS-passivated perovskite film. The concentration of electronic trap states and the hole mobility were then evaluated by measuring the *I-V* response in the space-charge-limited current (SCLC) regime (Figure 3b,c and *Supplementary Note 2*). The hole-only device with the CPS-treated perovskite absorber exhibits a lower trap density ($N_{trap} = 2.1 \times 10^{16}$ cm^{-3}) and higher hole mobility ($\mu_{hole} = 4.1 \times 10^{-3}$ cm^2 V^{-1} s^{-1}) than the pristine perovskite-based device ($N_{trap} = 6.1 \times 10^{16}$ cm^{-3} and $\mu_{hole} = 1.7 \times 10^{-3}$ cm^2 V^{-1} s^{-1}).

To characterize the interfacial charge transfer, electrochemical impedance spectroscopy (EIS) measurements were performed in the dark at a bias of 0.85 V (Figure 3d). In the EIS plots, the *x*-axis intersection at high frequency represents the total series resistance of the device, R_s, while the semicircle in the low-frequency region relates to the recombination resistance, R_{rec}.[22] The CPS-treated device has a smaller R_s (18.6 Ω) than the control device (31.3 Ω), which suggests that the CPS treatment improves the device conductivity and can result in higher FF.[23] The CPS treatment induces a significant increase in R_{rec} from 1.7 kΩ to 13.5 kΩ; we note that, since a larger R_{rec} value points to reduced carrier recombination, the CPS treatment alleviates interfacial charge loss. Figure S13 presents the Nyquist and Bode plots of intensity-modulated photocurrent spectroscopy (IMPS) for devices without and with CPS treatment. The charge carrier transport time τ_{tr} can be derived from $\tau_{tr} = 1/(2\pi \cdot f_{IMPS})$ where f_{IMPS} is the maximum at a certain light intensity in each semicircle. The CPS-treated device has shorter τ_{tr} than the control device, indicating a faster collection of charges at the electrodes (Figure 3e). The carrier diffusion coefficient D can be calculated via $D = d^2/(2.35\tau_{tr})$, where d is the thickness of the photoelectrode (Figure S14).[12,24] The D values of the CPS-treated device are higher than those of the control device under different light intensities (Figure 3f), which means that the photogenerated charges can more rapidly diffuse from the perovskite layer to the electrodes and be collected.

We also evaluated the PSC photovoltaic performance with the perovskite film treated with CPS solutions of different concentrations (Figure S15). As the CPS concentration increases from 0 to 40 mM, the device performance progressively improves. However, further increasing the concentration to 100 mM decreases the PCE, which can be attributed to the insulating nature of CPS and the adverse impact of thicker passivation layers.[25]

To further explore the impact of the nature of the passivation layer, two additional silane molecules, that is, CMS and tetramethoxysilane (TMS) (Figure S1), were also employed to coat the perovskite film. Compared to CPS, CMS contains a Cl atom yet with a shorter alkyl chain, while TMS has no Cl substitution. In a way similar to the CPS-treated devices, CMS passivation results in improved performance over the control devices, with J_{SC} of 24.4 mA cm^{-2}, V_{OC} of 1.13 V, *FF* of 72%, and *PCE* of 19.9% for the champion device (Figure S16). The average *PCE* over ten devices reaches 19.1 ± 0.5% (Figure S17). Importantly, compared to CPS-treated (maximum *PCE* = 20.3%) and CMS-treated (maximum *PCE* = 19.9%) devices, TMS-treated devices do not provide a substantial improvement (*PCE* = 17.8%) over the control device (*PCE* = 17.1%). These results highlight the importance of the presence of Cl in CPS and CMS in passivating the perovskite and enhancing device performance.

Hybrid perovskites are known to be chemically unstable in the presence of moisture and under illumination.[26] We studied the impact of moisture on pristine and CPS-treated PSCs by exposing the cells in a desiccator to a constant 35% relative humidity for 30 days, followed by exposure to ambient atmosphere at ca. 65% humidity for 7 additional days. Figure 4a–d presents the normalized photovoltaic parameters as a function of time. After 37 days, the CPS-treated device exhibits a considerably higher PCE (12.9%) than the control cells (6.2%). Both devices experience a J_{SC} drop while the V_{OC} values remain quite stable when the devices are stored in the desiccator; upon exposing the devices to ambient atmosphere, however, the V_{OC} of the control device drops significantly compared to that of the CPS-treated device (grey regions in Figure 4b), which further confirms the improved humidity stability upon CPS treatment. In order to evaluate the water-resistivity change, the contact angles of the perovskite films without and with CPS treatment were tested (Figure S18). Contact angles of 43.2° and 61.6° were measured for the pristine and CPS-treated perovskite films, respectively, indicating an improved water resistance of the CPS-treated perovskite.

The XRD patterns of the control and CPS-treated perovskite films after storage in ambient atmosphere for 2 days are shown in Figure 4e; the characteristic peak of cubic PbI_2 at 12.7° was observed in the pristine perovskite, while no PbI_2 peak can be identified in the CPS-treated perovskite. This result highlights the occurrence of ion migration and decomposition in the pristine perovskite, a consequence of its low moisture stability, while surface modification provides improved resistance against moisture. This can be further corroborated by tracking the PL spectra of the pristine and CPS-treated perovskite films stored in ambient atmosphere (Figure 4f). As expected, the PL spectra remain nearly unchanged for the CPS-treated perovskite, while the pristine perovskite film undergoes a red-shift of the PL peak position over time due to halide segregation into halide-rich components that act as recombination centers.[4,27]

In addition to the impact of humidity, we also investigated the stability under illumination (Figure S19). The pristine perovskite film was also seen to display a red-shift of the PL peak position over time. This is consistent with reports that the mixed halide perovskites undergo ion migration and thus phase segregation under continuous illumination. This results in the formation of halide-rich domains with a smaller band gap and a red-shifted emission (Figure S19a).[28] In contrast, the PL spectra of the CPS-passivated perovskite film are much more stable under AM 1.5G irradiation.[4]

Conclusion

In summary, we have demonstrated an interfacial passivation strategy that allows us to engineer a perovskite absorber layer with a smaller crystallite surface roughness. The simple deposition of strongly polar chlorosilane-based

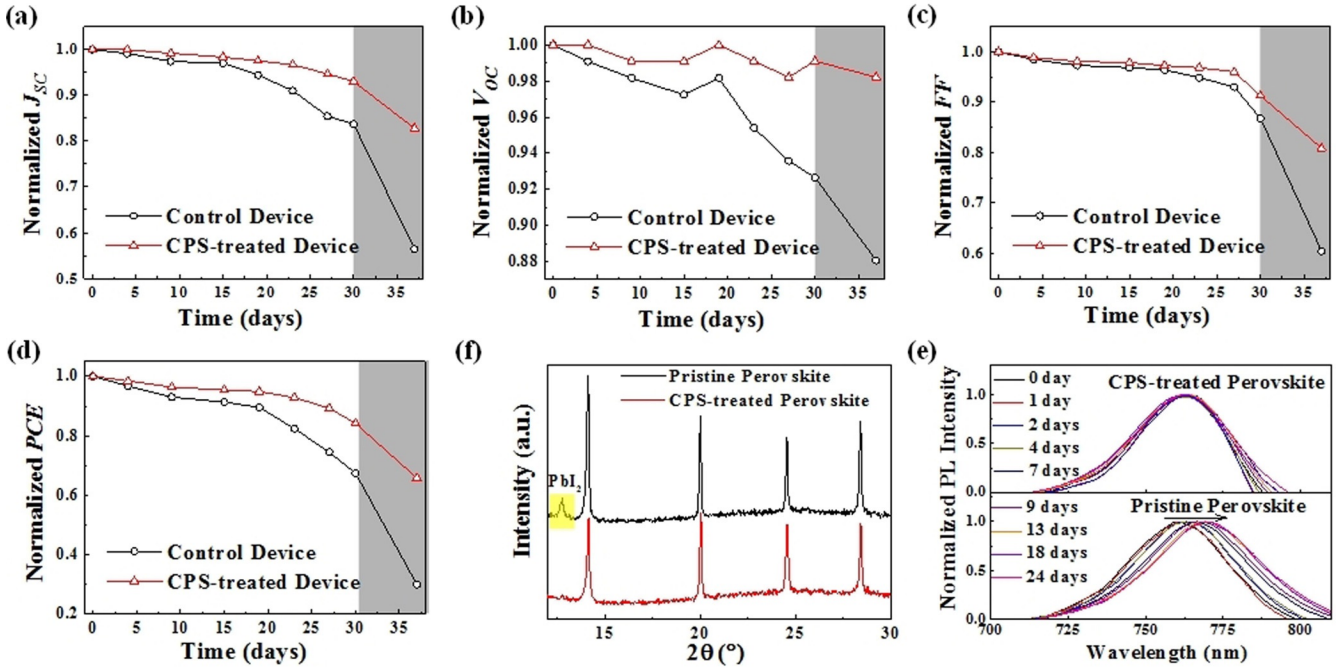

Figure 4. a)–d) Normalized photovoltaic parameters of PSCs before and after CPS treatment, exposed in desiccator for 30 days and then to ambient atmosphere for additional 7 days (grey area). e) XRD patterns of $Cs_{0.06}FA_{0.79}MA_{0.15}Pb(I_{0.85}Br_{0.15})_3$ without and with CPS treatment after storage in ambient atmosphere for 2 days. f) Photoluminescence from $Cs_{0.06}FA_{0.79}MA_{0.15}Pb(I_{0.85}Br_{0.15})_3$ films without and with CPS treatment, stored at ambient atmosphere.

molecules at the perovskite/Spiro-OMeTAD interface (i) results in an effective passivation of the perovskite defects, which contributes to suppress defect-induced non-radiative recombination processes, and (ii) improves the energy-level alignment at the perovskite/HTL interface, which increases the silane-cell performance. The chlorinated silane molecules bind to V_X-containing surfaces with their chlorine atoms pointing towards the V_I sites. The DFT results indicate that the chlorosilane molecules weakly adsorb on the perovskite surface with the chlorine atoms (partially) saturating the under-coordinated Pb cations to passivate the V_X sites. This arrangement of the silanes lowers the work function of the V_X-containing perovskite surface, to the extent of providing an Ohmic contact between the perovskite and the Spiro-OMeTAD HTL layer, which facilitates hole transfer across the interface. The CPS-treated perovskite absorber exhibits lower trap density ($N_{trap} = 2.1 \times 10^{16}\ cm^{-3}$) and higher hole mobility ($\mu_{hole} = 4.1 \times 10^{-3}\ cm^2 V^{-1} s^{-1}$) than the pristine perovskite-based device ($N_{trap} = 6.1 \times 10^{16}\ cm^{-3}$ and $\mu_{hole} = 1.7 \times 10^{-3}\ cm^2 V^{-1} s^{-1}$). The resulting CPS-treated device displays shorter charge carrier transport times and higher carrier diffusion coefficients, which points to a faster hole diffusion and collection from the perovskite layer to the electrode. As a result, a CPS-modified $Cs_{0.06}FA_{0.79}MA_{0.15}Pb(I_{0.85}Br_{0.15})_3$ device achieves a PCE of 20.3%, a nearly 20% increase over a device based on a pristine film. The same holds true for a $MAPbI_3$ device upon the CPS treatment. Importantly, the defect passivation by chlorinated silane molecules also improves the device stability by inhibiting phase segregation in humid air and under illumination.

Our study highlights the effectiveness of the interfacial deposition of polar silane molecules in providing defect passivation and control over interfacial energy-level alignment. By extension, the use of other halide-terminated molecules with a strong dipole moment as interfacial modifier can open up new avenues for the engineering of a variety of high-performance optoelectronic devices, including solar cells, photodetectors, or light-emitting diodes.

Acknowledgements

This work was supported by the NSF (CMMI 1914713, ECCS 1914562, DMR 1903990), the Natural Science Foundation of Jiangsu Province (BK20201202), the Department of the Navy, Office of Naval Research (Award No. N00014-20-1-2110), and the College of Science of the University of Arizona.

Conflict of Interest

The authors declare no conflict of interest.

Keywords: chlorosilane molecules · defect passivation · dipole moment · interface energy level alignment · perovskite solar cells

[1] National Renewable Energy Laboratory (NREL) **2021**.
[2] a) H. R. Tan, A. Jain, O. Voznyy, X. Z. Lan, F. P. G. de Arquer, J. Z. Fan, R. Quintero-Bermudez, M. J. Yuan, B. Zhang, Y. C.

Zhao, F. J. Fan, P. C. Li, L. N. Quan, Y. B. Zhao, Z. H. Lu, Z. Y. Yang, S. Hoogland, E. H. Sargent, *Science* **2017**, *355*, 722 – 726; b) X. P. Zheng, B. Chen, J. Dai, Y. J. Fang, Y. Bai, Y. Z. Lin, H. T. Wei, X. C. Zeng, J. S. Huang, *Nat. Energy* **2017**, *2*, 17102.

[3] W. S. Yang, B. W. Park, E. H. Jung, N. J. Jeon, Y. C. Kim, D. U. Lee, S. S. Shin, J. Seo, E. K. Kim, J. H. Noh, S. I. Seok, *Science* **2017**, *356*, 1376 – 1379.

[4] M. Abdi-Jalebi, Z. Andaji-Garmaroudi, S. Cacovich, C. Stavrakas, B. Philippe, J. M. Richter, M. Alsari, E. P. Booker, E. M. Hutter, A. J. Pearson, S. Lilliu, T. J. Savenije, H. Rensmo, G. Divitini, C. Ducati, R. H. Friend, S. D. Stranks, *Nature* **2018**, *555*, 497 – 501.

[5] a) P. Calado, A. M. Telford, D. Bryant, X. E. Li, J. Nelson, B. C. O'Regan, P. R. F. Barnes, *Nat. Commun.* **2016**, *7*, 13831; b) Y. C. Shao, Y. J. Fang, T. Li, Q. Wang, Q. F. Dong, Y. H. Deng, Y. B. Yuan, H. T. Wei, M. Y. Wang, A. Gruverman, J. Shielda, J. S. Huang, *Energy Environ. Sci.* **2016**, *9*, 1752 – 1759.

[6] a) S. Yang, J. Dai, Z. H. Yu, Y. C. Shao, Y. Zhou, X. Xiao, X. C. Zeng, J. S. Huang, *J. Am. Chem. Soc.* **2019**, *141*, 5781 – 5787; b) B. Wang, M. Zhang, X. Cui, Z. W. Wang, M. Rager, Y. K. Yang, Z. G. Zou, Z. L. Wang, Z. Q. Lin, *Angew. Chem. Int. Ed.* **2020**, *59*, 1611 – 1618; *Angew. Chem.* **2020**, *132*, 1628 – 1635; c) B. Wang, J. Iocozzia, M. Zhang, M. D. Ye, S. C. Yan, H. L. Jin, S. Wang, Z. G. Zou, Z. Q. Lin, *Chem. Soc. Rev.* **2019**, *48*, 4854 – 4891; d) H. Zhu, Y. Ren, L. Pan, O. Ouellette, F. T. Eickemeyer, Y. Wu, X. Li, S. Wang, H. Liu, X. Dong, S. M. Zakeeruddin, Y. Liu, A. Hagfeldt, M. Grätzel, *J. Am. Chem. Soc.* **2021**, *143*, 3231 – 3237.

[7] S. H. Wang, T. Sakurai, W. J. Wen, Y. B. Qi, *Adv. Mater. Interfaces* **2018**, *5*, 1800260.

[8] P. J. Hang, J. S. Xie, G. Li, Y. Wang, D. S. Fang, Y. X. Yao, D. Y. Xie, C. Cui, K. Y. Yan, J. B. Xu, D. R. Yang, X. G. Yu, *iScience* **2019**, *21*, 217.

[9] D. W. de Quilettes, S. M. Vorpahl, S. D. Stranks, H. Nagaoka, G. E. Eperon, M. E. Ziffer, H. J. Snaith, D. S. Ginger, *Science* **2015**, *348*, 683 – 686.

[10] R. Long, J. Liu, O. V. Prezhdo, *J. Am. Chem. Soc.* **2016**, *138*, 3884 – 3890.

[11] A. S. Hassanien, A. A. Akl, *J. Alloys Compd.* **2015**, *648*, 280 – 290.

[12] M. He, B. Li, X. Cui, B. B. Jiang, Y. J. He, Y. H. Chen, D. O'Neil, P. Szymanski, M. A. El-Sayed, J. S. Huang, Z. Q. Lin, *Nat. Commun.* **2017**, *8*, 16045.

[13] H. L. Tan, X. M. Wen, R. Amal, Y. H. Ng, *J. Phys. Chem. Lett.* **2016**, *7*, 1400 – 1405.

[14] D. Y. Son, J. W. Lee, Y. J. Choi, I. H. Jang, S. Lee, P. J. Yoo, H. Shin, N. Ahn, M. Choi, D. Kim, N. G. Park, *Nat. Energy* **2016**, *1*, 16081.

[15] a) S. H. Cho, Y. U. Lee, J. S. Lee, K. M. Jo, B. S. Kim, H. S. Kong, J. Y. Kwon, M. K. Han, *J. Disp. Technol.* **2012**, *8*, 35 – 40; b) S. Kobayashi, T. Nishikawa, T. Takenobu, S. Mori, T. Shimoda, T. Mitani, H. Shimotani, N. Yoshimoto, S. Ogawa, Y. Iwasa, *Nat. Mater.* **2004**, *3*, 317 – 322.

[16] N. T. Plymale, A. A. Ramachandran, A. Lim, B. S. Brunschwig, N. S. Lewis, *J. Phys. Chem. C* **2016**, *120*, 14157 – 14169.

[17] a) S. Q. Tan, N. Zhou, Y. H. Chen, L. Li, G. L. Liu, P. F. Liu, C. Zhu, J. Z. Lu, W. T. Sun, Q. Chen, H. P. Zhou, *Adv. Energy Mater.* **2019**, *9*, 1803024; b) E. M. J. Johansson, R. Scholin, H. Siegbahn, A. Hagfeldt, H. Rensmo, *Chem. Phys. Lett.* **2011**, *515*, 146 – 150; c) K. G. Lim, S. Ahn, T. W. Lee, *J. Mater. Chem. C* **2018**, *6*, 2915 – 2924.

[18] W. J. Yin, T. T. Shi, Y. F. Yan, *Appl. Phys. Lett.* **2014**, *104*, 063903.

[19] N. J. Jeon, H. Na, E. H. Jung, T. Y. Yang, Y. G. Lee, G. Kim, H. W. Shin, S. I. Seok, J. Lee, J. Seo, *Nat. Energy* **2018**, *3*, 682.

[20] a) G. Heimel, L. Romaner, E. Zojer, J. L. Bredas, *Acc. Chem. Res.* **2008**, *41*, 721 – 729; b) H. Li, P. Winget, J. L. Bredast, *Chem. Mater.* **2014**, *26*, 631 – 646.

[21] R. L. Grimm, M. J. Bierman, L. E. O'Leary, N. C. Strandwitz, B. S. Brunschwig, N. S. Lewis, *J. Phys. Chem. C* **2012**, *116*, 23569 – 23576.

[22] X. T. Meng, X. Cui, M. Rager, S. G. Zhang, Z. W. Wang, J. Yu, Y. W. Harn, Z. T. Kang, B. K. Wagner, Y. Liu, C. Yu, J. S. Qiu, Z. Q. Lin, *Nano Energy* **2018**, *52*, 123 – 133.

[23] a) L. B. Xiong, M. C. Qin, G. Yang, Y. X. Guo, H. W. Lei, Q. Liu, W. J. Ke, H. Tao, P. L. Qin, S. Z. Li, H. Q. Yu, G. J. Fang, *J. Mater. Chem. A* **2016**, *4*, 8374 – 8383; b) W. Q. Wu, Q. Wang, Y. J. Fang, Y. C. Shao, S. Tang, Y. H. Deng, H. D. Lu, Y. Liu, T. Li, Z. B. Yang, A. Gruverman, J. S. Huang, *Nat. Commun.* **2018**, *9*, 1625.

[24] U. Poudyal, F. S. Maloney, K. Sapkota, W. Y. Wang, *Nanotechnology* **2017**, *28*, 415401.

[25] a) Y. H. Zhou, C. Fuentes-Hernandez, J. Shim, J. Meyer, A. J. Giordano, H. Li, P. Winget, T. Papadopoulos, H. Cheun, J. Kim, M. Fenoll, A. Dindar, W. Haske, E. Najafabadi, T. M. Khan, H. Sojoudi, S. Barlow, S. Graham, J. L. Bredas, S. R. Marder, A. Kahn, B. Kippelen, *Science* **2012**, *336*, 327 – 332; b) Z. L. Chen, Q. F. Dong, Y. Liu, C. X. Bao, Y. J. Fang, Y. Lin, S. Tang, Q. Wang, X. Xiao, Y. Bai, Y. H. Deng, J. S. Huang, *Nat. Commun.* **2017**, *8*, 1890.

[26] C. C. Boyd, R. Cheacharoen, T. Leijtens, M. D. McGehee, *Chem. Rev.* **2019**, *119*, 3418 – 3451.

[27] E. T. Hoke, D. J. Slotcavage, E. R. Dohner, A. R. Bowring, H. I. Karunadasa, M. D. McGehee, *Chem. Sci.* **2015**, *6*, 613 – 617.

[28] a) G. F. Samu, C. Janaky, P. V. Kamat, *ACS Energy Lett.* **2017**, *2*, 1860 – 1861; b) T. A. Berhe, W. N. Su, C. H. Chen, C. J. Pan, J. H. Cheng, H. M. Chen, M. C. Tsai, L. Y. Chen, A. A. Dubale, B. J. Hwang, *Energy Environ. Sci.* **2016**, *9*, 323 – 356.

Manuscript received: April 22, 2021
Accepted manuscript online: June 9, 2021
Version of record online: June 30, 2021

